

# 3D printed patient-specific thorax phantom with realistic heterogenous bone radiopacity using filament printer technology

Sepideh Hatamikia<sup>a,b,c,\*</sup>, Gernot Kronreif<sup>a</sup>, Alexander Unger<sup>a</sup>, Gunpreet Oberoi<sup>c</sup>, Laszlo Jaksa<sup>a</sup>, Ewald Unger<sup>c</sup>, Stefan Koschitz<sup>a</sup>, Ingo Gulyas<sup>d</sup>, Nikolaus Irnstorfer<sup>e</sup>, Martin Buschmann<sup>d</sup>, Joachim Kettenbach<sup>f</sup>, Wolfgang Birkfellner<sup>c</sup>, Andrea Lorenz<sup>a</sup>

<sup>a</sup> Austrian Center for Medical Innovation and Technology, Wiener Neustadt, Austria

<sup>b</sup> Danube Private University, 3500 Krems an der Donau, Austria

<sup>c</sup> Center for Medical Physics and Biomedical Engineering, Medical University of Vienna, Vienna, Austria

<sup>d</sup> Department of Radiation Oncology, Medical University of Vienna, Vienna, Austria

<sup>e</sup> Division of Nuclear Medicine, Department of Biomedical Imaging and Image-guided Therapy at the Medical University of Vienna

<sup>f</sup> Institute of Diagnostic, Interventional Radiology and Nuclear Medicine, Landeskrankenhaus Wiener Neustadt, Wiener Neustadt, Austria

Received 15 October 2021; accepted 1 February 2022

## Abstract

*Current medical imaging phantoms are usually limited by simplified geometry and radiographic skeletal homogeneity, which confines their usage for image quality assessment. In order to fabricate realistic imaging phantoms, replication of the entire tissue morphology and the associated CT numbers, defined as Hounsfield Unit (HU) is required. 3D printing is a promising technology for the production of medical imaging phantoms with accurate anatomical replication. So far, the majority of the imaging phantoms using 3D printing technologies tried to mimic the average HU of soft tissue human organs. One important aspect of the anthropomorphic imaging phantoms is also the replication of realistic radiodensities for bone tissues. In this study, we used filament printing technology to develop a CT-derived 3D printed thorax phantom with realistic bone-equivalent radiodensity using only one single commercially available filament. The generated thorax phantom geometry closely resembles a patient and includes direct manufacturing of bone structures while creating life-like heterogeneity within bone tissues. A HU analysis as well as a physical dimensional comparison were performed in order to evaluate the density and geometry agreement between the proposed phantom and the corresponding CT data. With the achieved density range (-482 to 968 HU) we could successfully mimic the realistic radiodensity of the bone marrow as well as the cortical bone for the ribs, vertebral body and dorsal vertebral column in the thorax skeleton. In addition, considering the large radiodensity range achieved a full thorax imaging phantom mimicking also soft tissues can become feasible. The physical dimensional comparison using both Extrema Analysis and Collision Detection methods confirmed a mean surface overlap of 90% and a mean volumetric overlap of 84,56% between the patient and phantom model. Furthermore, the reproducibility analyses revealed a good geometry and radiodensity duplicability in 24 printed cylinder replicas. Thus, according to our results, the proposed additively manufactured anthropomorphic thorax phantom has the potential to be efficiently used for validation of imaging- and radiation-based procedures in precision medicine.*

**Keywords:** Imaging phantom, 3D printing, Patient-specific thorax phantom, Heterogenous bone radiopacity, Filament printer technology

\*Corresponding author: Sepideh Hatamikia, Austrian Center for Medical Innovation and Technology, Wiener Neustadt, Austria / Danube Private University, Krems an der Donau, Austria / Center for Medical Physics and Biomedical Engineering, Medical University of Vienna, Austria.

E-mail: [sepideh.hatamikia@acmit.at](mailto:sepideh.hatamikia@acmit.at) (S. Hatamikia).

## 1 Introduction

Medical Imaging phantoms are widely used for validation and verification of surgical guidance, diagnostic imaging, and radiation oncology procedures [1,2]. In order to fabricate realistic phantoms for such procedures, the manufactured phantoms need to replicate the entire tissue morphology and the associated CT numbers, defined as Hounsfield Unit (HU). Additive Manufacturing (AM) technology, colloquially called 3D printing, provides an inexpensive opportunity for accurate anatomical replication with customization capabilities [3–5].

So far, 3D printing technologies have been extensively employed to mimic soft tissue human organs for both imaging and dosimetry phantoms [6]. However, one important aspect of anthropomorphic phantoms is also the replication of realistic radiodensities for bone tissue. There are several applications where medical imaging phantoms with real-life bone structures are required. For instance, this is particularly important for verification of advanced image reconstruction techniques. Bony tissues are considered as highly attenuation structures, which significantly affect the contrast of structures which are in proximity to bones in the reconstructed 3D image [7]. Therefore, simplified phantoms with non-realistic radiation attenuation properties for bony structures can lead to an inaccurate verification of such image reconstruction algorithms. In addition, in other applications such as orthovoltage, superficial electron beam radiotherapy as well as low energy brachytherapy having realistic bones in the phantom is of great importance, as bones can be in vicinity to the tumor and therefore interfere with the required dose distribution for the patient [8]. Verification of new image segmentation, rib suppression and 2D/3D image registration methods are other important clinical image processing techniques, where having phantoms with realistic HU for bone is essential, as validation of such imaging techniques fully rely on the accuracy and reproducibility of these phantoms [9–11].

Several studies have been done in order to fabricate bone-equivalent phantoms. The authors in [12] have developed a template for a 3D printed brain model using a high-density plaster of Paris as a skull substitute for verification of image segmentation. In another study, using material jetting technology, shell compartments filled with Vaseline and Dipotassium phosphate coated with gypsum as bone marrow substitutes were fabricated to mimic the cortical bone radiodensity [13,14]. All aforementioned approaches used an indirect manufacturing process to produce the bone-equivalent phantoms. However, a direct manufacturing process of such bone-like phantoms is desirable due to lack of requirement to multiple processing stages.

By now, only few studies have proposed a direct replication of bones in patient-specific 3D printed phantoms, mainly using different filament materials and Fused Deposition Modelling (FDM) technology. In a study [15], 14 available commercial filaments were investigated regarding

their radiation attenuation property in order to access their usage in 3D printed phantoms for computed tomography. Using these filaments all human tissues could be mimicked except cortical bone above a density of  $\sim 350$  HU. In another study [16] authors proposed a 3D printed phantom in which the soft tissues were fabricated from ABS (Acrylnitril-Butadien-Styrol) material and a mixture of ABS with 100% infill density and bismuth powder was used for the replication of the bones. However, their results exhibited a very high range between 1000 to 3000 HU which is limited to replicate only cortical bone. In [17] authors developed a mixture of ABS filament reinforced with Barium sulphate in order to emulate both cortical and the cancellous bones. The resulting mean HU using a linear grid infill for cortical bone was 944 using full infill density and for cancellous bones were 184 and 92 using infill density of 20% and 10%, respectively. However, the usage of a much lower than 100% infill density for cancellous bones led to presence of the printed grid and air gaps in the standard CT scan. In another study [18] authors proposed the use of a dual-head printer with two different filaments PLA and StoneFil PLA-concrete at several different infill densities in order to achieve 3D printing materials with equivalent radiodensity as muscle, lung and bone. They were able to produce densities from 300 to 630 HU similar to inner and cortical bone. Using the same filaments, another research group [8] proposed a method to control the filament extrusion rate during the 3D printing process. Using this approach, they could achieve an average of  $523 \pm 259$  HU while mimicking a realistic distribution of HU as in the patient CT data.

Some studies also have tried to propose realistic thorax phantoms using different 3D printing technologies. Mayer et al. [19] used a PolyJet3D printer using Tango Plus and Vero White materials to develop a thorax phantom. The achieved HU was lower than the human bone of 200–1000 HU. Another researcher [20] proposed a breathing thorax phantom consisting of the internal organs with simplified shapes using ABS in which ribs were carved and then filled with a mixture of calcium sulfate dehydrate. Another thorax 3D printed phantom with multiple tissue types and radiodensities to resemble a CT from a patient with lung cancer was proposed in [21]. The Gypsum material was used to fabricate the bony structures which were printed using a PolyJet<sup>TM</sup> 3D printer. Rance et al. [22] proposed an interlace deposition method by taking advantage of the dual-extrusion printing technology and used two different filaments including polylactic-acid (PLA) and iron-reinforced PLA (Fe-PLA) in order to enable the emulation of bone-like HU. In addition, the authors in [22] developed a modular, anthropomorphic CT and MR thorax phantom including liver, ribs, lung and additional tracking spheres. The fabricated modules could simulate HU, T1 and T2 values comparable to corresponding human tissues. The rib cage module consists made of a calcium carbonate ( $\text{CaCO}_3$ ) which could be inserted on top of lung and liver modules. However, the simplicity of the bone model [19–23], the non-realistic HU range

achieved, and discrepancies achieved between the mean HU for 3D printed bone parts compared to the target HUs were the limitations of these studies [19–21,23].

In a previous study [4] we proposed a CT-based modified PolyJet 3D printing technique to print a hollow thorax phantom replicating skeletal morphology of the patient. The printed hollow phantom was then filled by a novel radiopaque amalgamate replicating the bone density in specific regions. The proposed technique in [4] could enhance previous studies [19–22] by manufacturing realistic bone model and realistic HU values inside the thorax phantom. In addition, a good agreement between the mean HU values in the proposed phantom compared to the target patient thorax CT scan was achieved. Despite all the achieved improvements in [4], the proposed method revealed several limitations. This approach included a difficult cleaning process, required several steps in manufacturing of the bone and could not mimic the internal bone structures, including cortical (compact) bone and bone marrow. In addition, the process of filling the phantom by radiopaque amalgamate introduced air bubbles in the entire phantom which led to artefacts in the images. The current study tries to overcome the limitations reported in [4] and focuses mainly on simulating realistic bone tissues in an imaging thorax phantom.

The aim of this study was to develop a CT-based anthropomorphic thorax phantom with realistic heterogeneous skeletal radiation attenuation properties, which could be manufactured directly by 3D printing technology using one single commercially available filament, without the need of a cleaning process. In particular, the compact bone and bone marrow can be 3D printed in a reasonably realistic arrangement as in the human CT. The performance of the phantom was evaluated by a comparison of HU values and physical dimensions to the corresponding CT data. In addition, the full radiodensity spectrum, which could be achieved using such a filament, and its relation to real human bone and soft tissue densities, was investigated. A reproducibility analysis which guarantees the replicability of the proposed phantom was also performed.

## 2 Materials and Methods

The materials and methods section is organized as follow: First, an evaluation of the HU range corresponding to the patient CT data is reported (Section 2.1), then the phantom design is explained (Section 2.2) and the filament printing technique used is described (Section 2.3). Creation of test samples with specific radiation attenuation properties and the selected HUs to be used in the thorax phantom are presented in Section 2.4 and 2.5, respectively. In addition, the additive manufacturing process of the thorax phantom is described in Section 2.6 and reproducibility tests are explained in Section 2.7. HU analysis and the physical dimensional comparison method are also described in Section 2.8 and 2.9, respectively.

### 2.1 Determination of realistic HU range in patient CT data

The patient data used in this study was approved by the Ethics Committee of the Medical University of Vienna (EK1253/2012) [4]. This patient CT data (SOMATOM Definition AS, Siemens Healthineers, Erlangen Germany, tube voltage 120 kVp, tube current time product 315 mAs, pixel spacing 0.98 mm) includes a total of 176 Digital Imaging and Communication in Medicine (DICOM) data files. We investigated the HU values related to the bone marrow of the patient thorax CT and found three areas with different radiodensities; these three areas were inside the ribs, vertebral body and dorsal vertebral column (Fig. 1) [4]. In the real patient CT, average density values (Section 2.8) achieved were 20, 107 and 184 HU for the bone marrow, corresponding to vertebral body, ribs and dorsal vertebral column, respectively. We also evaluated HU range and thickness aspects of the cortical bone of the patient thorax skeleton in the CT scan. Different thicknesses of the cortical bone were calculated (Section 2.7) in these three different areas (approximately 1 mm, 2 mm and 2.5 mm for the vertebral body, ribs and dorsal vertebral column, respectively) (Fig. 1). In addition, the density range of the cortical bone in the patient CT (Section 2.8) was between 230 HU and 1200 HU.

### 2.2 Three-Dimensional (3D) Phantom Design

The phantom design is based on the same dataset as in [4], which was derived from the CT scan (Section 2.1) and initially segmented using Materialize Mimics Research 21.0 software (Materialize, Leuven, Belgium). The scan depicted the whole thorax, including the ribs, thoracic spine, and sternum. The original data was further processed using 3D-Slicer software [28,29]. In contrast to the original data, the bones were not hollowed, the surrounding soft tissue layer was reduced to enlarge the interior space, and the length of the thorax was shortened to shorten printing time. In addition, a flat bearing was added dorsally to facilitate the mounting in the CT scan. Furthermore, the bones were separated into the three parts (Section 2.1), based on their imaging properties: vertebral body, dorsal vertebral column and ribs (Fig. 2).

### 2.3 Additive manufacturing using filament printing technology

In FDM technology, the object is generated layer-wise, extruding a filament through a nozzle. This allows for a large variety of patterns. As usually only the outer surface of the object is important, the contour is built with a certain number of lines, the so-called perimeters, and filled up with some kind of grid, which is called infill, where the pattern can be chosen, and the density can be set in %. This procedure reduces material, weight and printing time while still guaranteeing a certain level of stability and printability. On the

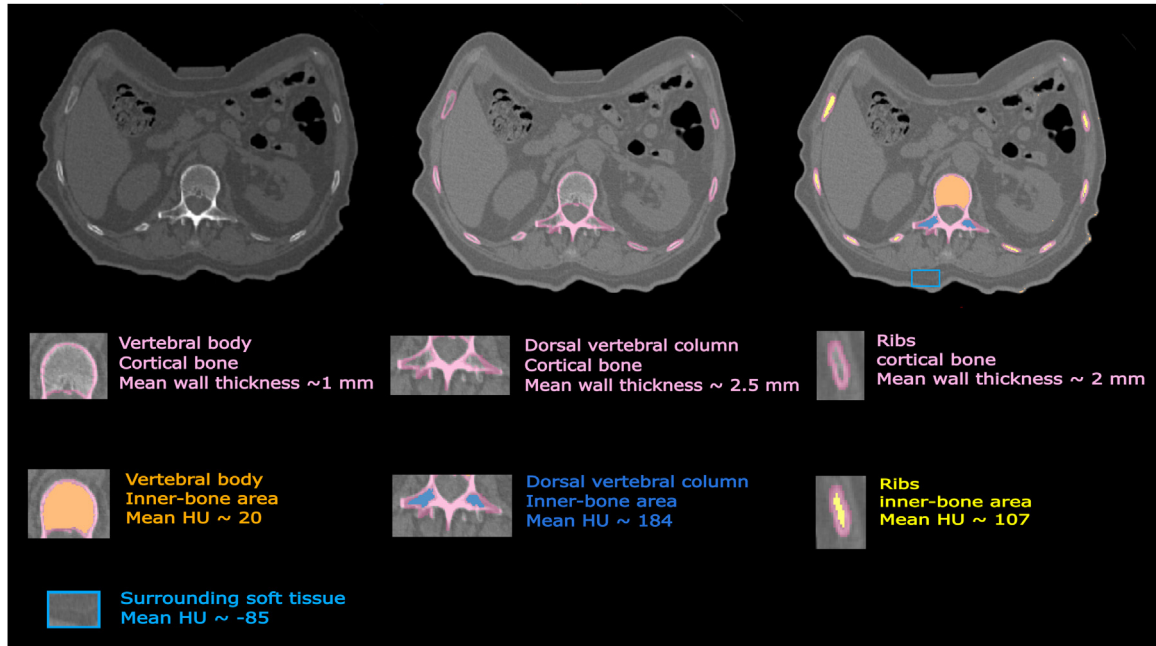


Figure 1. Representation of different heterogeneity of bone density inside one axial slice of the patient CT. The thicknesses of the cortical bone were approximately 1 mm, 2 mm and 2.5 mm for the vertebral body, ribs and dorsal vertebral column, respectively. Average density values were 20, and 107, 184 and -85 HU for bone marrow areas, corresponding to vertebral body, ribs, dorsal vertebral column and surrounding soft tissue respectively.

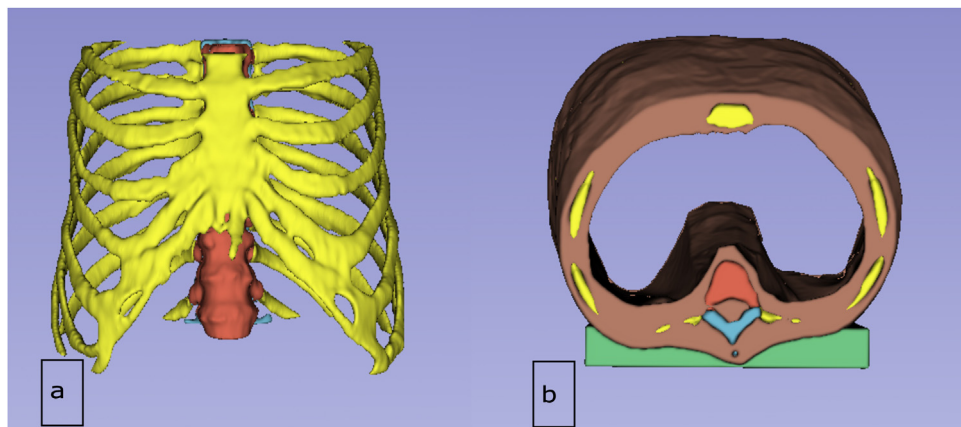


Figure 2. Representation of the designed phantom in 3D Slicer software, a) Anterior view, b) Caudal view. Vertebral body, dorsal vertebral column, ribs, soft tissue and flat bearing are shown in red, blue, yellow, brown and green respectively.

other hand, it creates ideal possibilities for mimicking bone tissue, where the wall thickness of the cortical bone can be reproduced by the number of perimeters and the density of the spongy bone with the density of the infill. As the feature size of the infill pattern can be chosen below the standard CT resolution, the grid will not be visible in the CT-image for a large range of infill densities, but different densities will result in different grey values, making this procedure perfectly fitting for the generation of CT phantoms of human bone.

#### 2.4 Creation of samples with specific radiation attenuation properties

In order to determine the infill densities that reproduce different radiodensities, we varied the infill density parameter of the print using FDM technology and StoneFil material. A cylinder model with the length of 7 cm and diameter of 2 cm was created for the test printing. A set of different infill densities including 100%, 95%, 90%, 85%, 80%, 75%, 70% filling (labeled as samples S0-S6) and 65%, 60%, 55%, 50%,

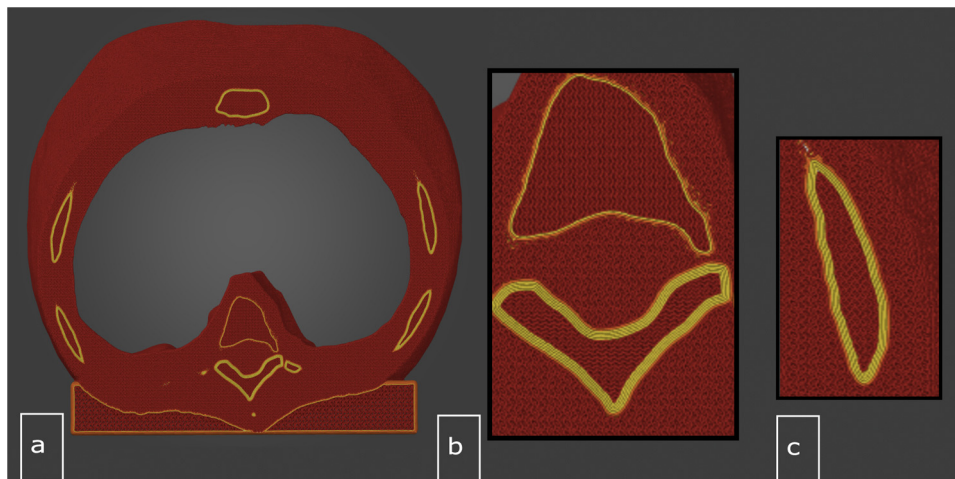


Figure 3. Illustration of the design of the cortical bone in the PrusaSlicer, a) Cranio-caudal view. Magnification view of b) vertebral body and dorsal vertebral column c) ribs.

45%, 40% filling (labeled as samples S7-S12) and 35%, 30%, 25%, 20%, 15%, 10% filling (labeled as samples S13-S18) was used to imitate a gradient in HU range within three printed cylinders. The 3D-printing was done at Austrian Center for Medical Innovation and Technology (ACMIT) using a commercial filament 3D-printer (Original Prusa i3 MK3S, Prusa Research a.s., Praha, Czech Republic) with a building platform of 25×21×21 cm. The G-Code for printing was prepared with the PrusaSlicer Software (PrusaSlicer 2.3.0, Prusa Research a.s., Praha, Czech Republic). A Gyroid pattern was used for the infill. The layer resolution was 0.2 mm for all samples. Printing temperature and speeds were selected according to the filament manufacturers and 3D printer specifications. The test printed cylinders were scanned using the same CT (Section 2.1) with the standard clinical CT protocol (tube voltage 120 kVp, tube current time product 315 mAs, slice thickness 2 mm, pixel spacing 0.68 mm) in order to evaluate their density properties. We also investigated the CT scan for smaller pixel spacing including 0.5 mm, 0.4 mm and 0.3 mm in order to check the visibility of the printed grid. In addition, an isotropic voxel size equal to 0.6 mm (both slice thickness and pixel spacing were set to 0.6 mm) was examined.

## 2.5 Density values selected to be replicated in the thorax phantom

In this study we propose to create complex bone-like heterogeneity inside a 3D printed thorax phantom. Radiodensities of the bone marrow inside the ribs, vertebral body and dorsal vertebral column in the patient thorax CT were replicated by samples S8, S7, S6 respectively, for the proposed 3D printed thorax phantom (Figs. 1 and 2). The selection of these three samples were done after matching the resulted HU values achieved from the cylinders CT with the corresponding CT values in the three mentioned areas in the patient scan. In

this study, we also used the infill density as in sample S9 to mimic the surrounding soft tissue (with average -85 HU) for embedding the thorax skeleton (Figs. 1 and 2).

## 2.6 Additive manufacturing of the thorax phantom

For the printing of the phantom, the thorax model had to be separated into 13 different parts to fit onto the building platform. In order to define different infill densities and number of perimeters for each part in PrusaSlicer (Fig. 3), the whole model was imported as one part and different sub-parts were added as modifiers. In this study, in order to simulate the cortical bone of the thorax phantom, we propose the periphery of the structures to be fully filled while inner structures to be partially filled, this happened to make the final print to be a more bone-like structure (Fig. 3). The process of manufacturing of the cortical bone included layer-by-layer printing (each perimeter approximately 0.45 mm) using full filled material (S0) until the desirable thickness was achieved. We used 2 (=0.9 mm), 4 (=1.8 mm), 5 (=2.25) perimeters in order to reach the approximate cortical bone thickness 1 mm, 2 mm and 2.5 mm for vertebral body, ribs and dorsal vertebral column, respectively (Figs. 1-3).

## 2.7 Reproducibility Tests

In order to investigate the reproducibility of the simulated radiopacity of our approach, we printed twenty-four replicas (twelve replication of S0-S12) of the cylinder model (Section 2.4). The average density values were calculated for all replicas at all different infill densities (Section 2.8). We also investigated the replicability of the simulated cortical bone thickness by printing solid contours surrounding the cylinders. The three different wall thicknesses (Section 2.6) including

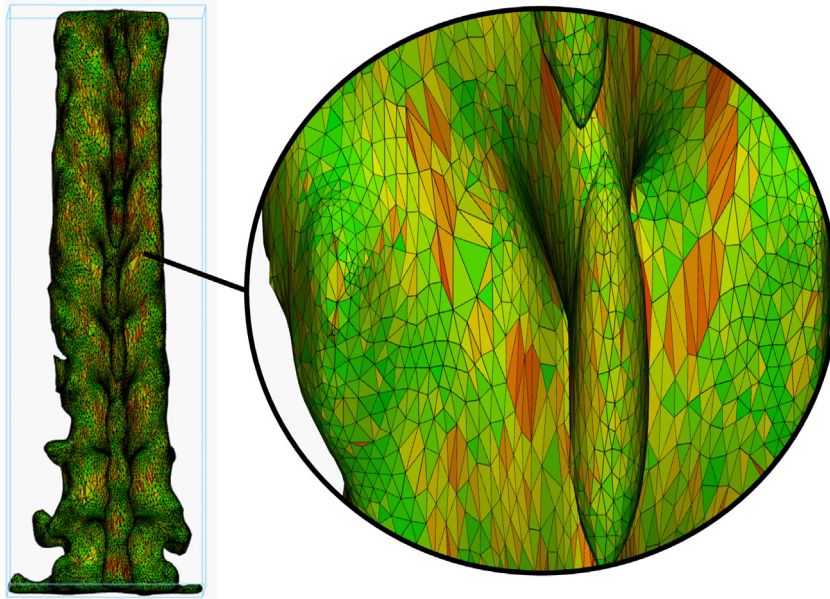


Figure 4. Workflow of physical dimensional analysis using the vertebral body as an example. Mesh refinement using Materialise-3-matic software.

0.9 mm, 1.8 mm, 2.25 mm were simulated (each thickness size was repeated for eight cylinders).

To evaluate the wall thickness of the replicas as well as the thicknesses of the cortical bone in the patient CT (Section 2.1) and the final thorax skeleton, we segmented the cortical bone using the 3D Slicer software and used the 3D Slicer fiducial tool to measure the thickness in millimeter. This measurement was repeated for several slices through the CT scan and finally an average and the standard deviation over all the achieved values are calculated for the corresponding area.

## 2.8 HU analysis of the patient and phantom thorax CT and test samples

We used the Analyze 12.0 toolkit (AnalyzeDirect, Overland Park, United States) in order to measure the HU values from the CT scan related to inner-bone areas inside the ribs, vertebral body and dorsal vertebral column for both patient and phantom thorax scan. For each of the three inner areas, we selected different line profiles inside the corresponding region and measured the HU by calculating the average and the standard deviation over all points for the selections related to those line profiles. In order to have an approximate over HU of the cortical bone inside the thorax skeleton, we used 3D Slicer software and segmented the cortical bony structures. A histogram of the HU spectrum was then computed from the segmented bone in order to estimate the HU range of the cortical bone tissue. Furthermore, to calculate the radiodensity from the CT of the cylinder prints, we used 3D Slicer software and cropped the CT volume (in cylinder shape with

radius 1 cm) at different region of interests (ROIs) each corresponding to the area with particular infill density (S0-S18). Then, Matlab software was used to calculate the average and standard deviation over the gray values for each cropped ROI and therefore HU values related to S0-S18 were calculated.

## 2.9 Physical dimensional comparison between the phantom and patient STL

We generated STL (Stereolithographic) files of the three skeletal parts from the thorax phantom CT and registered them to the respective STL files from the patient thorax CT. Subsequently, the parts were compared using Extrema Analysis for the surface overlap and Collision Detection for volume equivalence in 3-matic Research 13.0 software (Materialise, Leuven, Belgium). The former operation analyses extrema points (hill curvature of surface) based on the selection of the part in a specific axis ( $x$ ,  $y$ ,  $z$ ) direction. Within this operation are the possibilities to generate maximum, minimum, and both maximum and minimum extrema points. These points are visualized by different color codes to differentiate specific extrema points. In the latter operation, the analysis intersections (or collisions) occur between two parts and the colliding volume is calculated. To improve the visual output, the selected parts were advanced with a finer mesh (Fig. 4). The intersection between parts is visualized using marked triangles. An intersection part representing the colliding volume was created by Boolean intersection and the volume was calculated automatically.

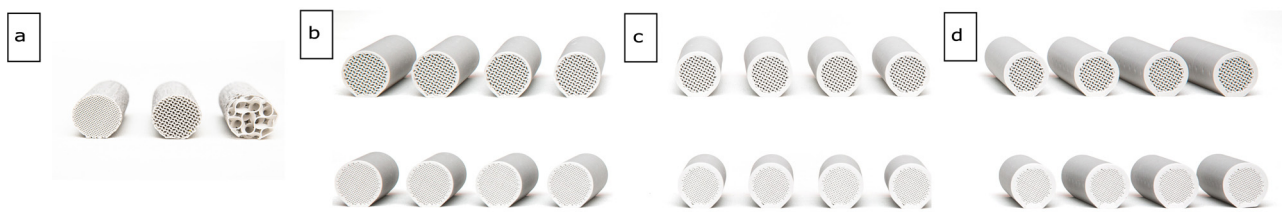


Figure 5. The three printed cylinders, S0-S6 (a, Left), S7-S12 (a, Middle), S13-S18 (a, Right), (b) the eight printed replicas (S0-S12) with 1 mm wall thickness, (c) eight replicas (S0-S12) with 2 mm wall thickness, and (d) the eight replicas (S0-S12) with 2.5 mm wall thickness.

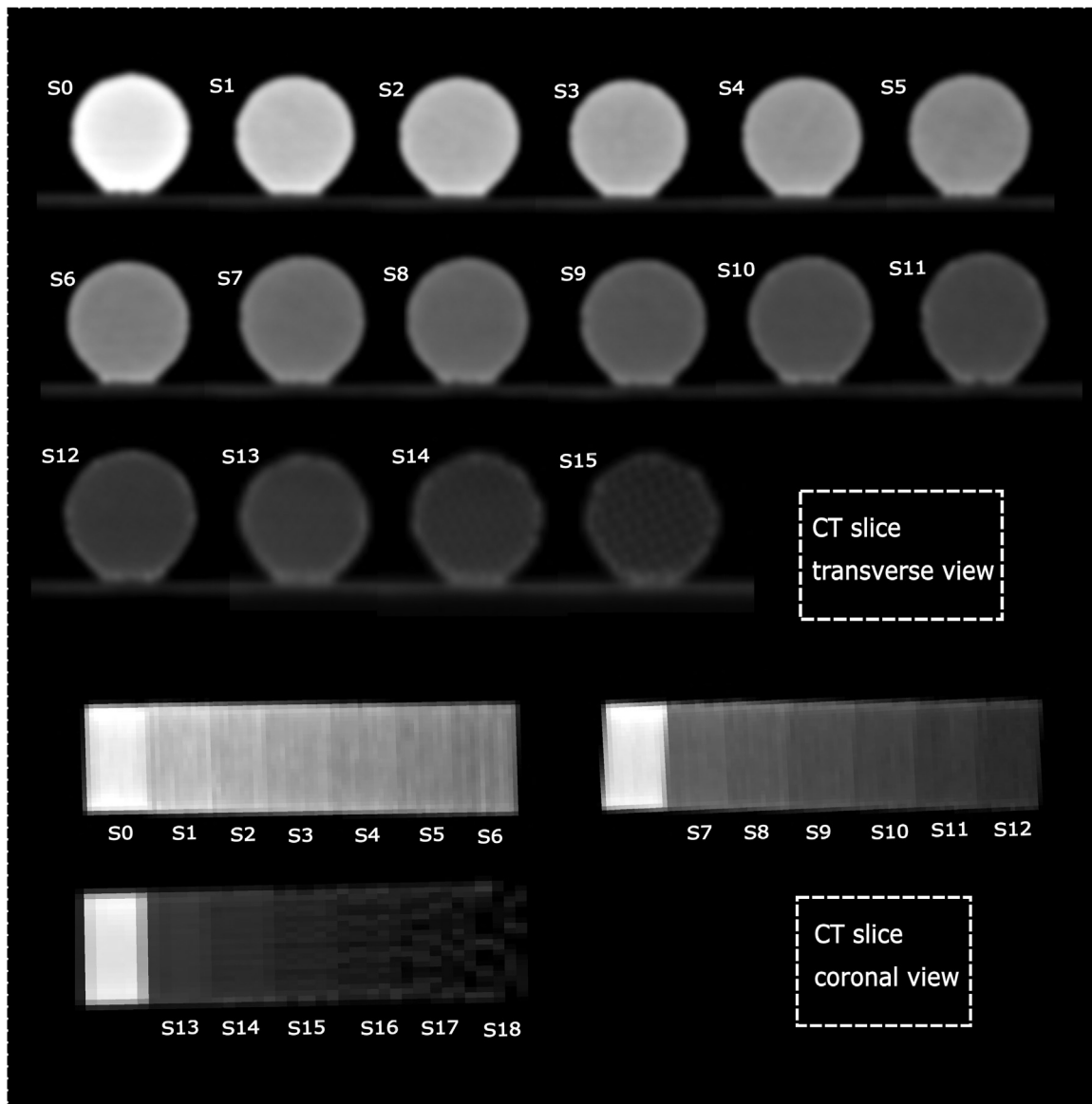


Figure 6. The transverse and coronal views from the CT scan from samples S0-S15.

Table 1

The resulting HU values achieved for samples S0-S14 for different infill densities, corresponding tissues with equivalence radiodensity [23,24]. The HU value for S15 is not considered in this study due to the visibility of the printed grid in the CT scan.

Sample	Infill density (%)	CT value (HU) (average $\pm$ standard deviation)	Corresponding Tissue
S0	100	968 $\pm$ 38	Compact bone
S1	95	669 $\pm$ 35	Compact bone
S2	90	572 $\pm$ 33	Compact bone
S3	85	464 $\pm$ 38	Compact bone, Bone marrow
S4	80	371 $\pm$ 32	Bone marrow
S5	75	278 $\pm$ 32	Organs, Bone marrow
S6	70	189 $\pm$ 38	Organs, Bone marrow, Muscle
S7	65	88 $\pm$ 22	Muscle, Organs, Bone marrow, Blood
S8	60	10 $\pm$ 25	Muscle, Organs, Blood
S9	55	-77 $\pm$ 19	Fat
S10	50	-146 $\pm$ 19	Fat, Skin
S11	45	-237 $\pm$ 23	Fat, Skin
S12	40	-314 $\pm$ 19	Skin
S13	35	-393 $\pm$ 28	Skin
S14	30	-482 $\pm$ 45	Lung, Skin
S15	25	-	-

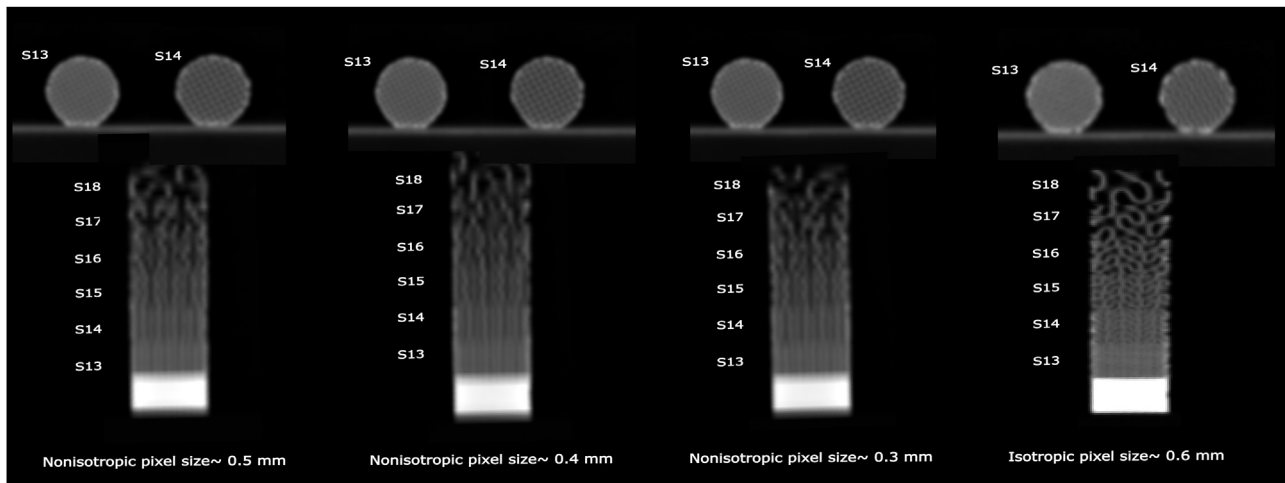


Figure 7. The transverse and coronal views from the CT scan from samples S13-S14 for non-isotropic pixel size with pixel sizes of 0.5 mm, 0.4 mm, 0.3 mm as well as isotropic pixel size equal to 0.6 mm.

### 3 Results

#### 3.1 Resulting density values for the printed cylinders

The three test cylinders with infill density S0-S18 (Section 2.4) as well as cylinders for reproducibility analysis (Section 2.7) were printed successfully (Fig. 5). The CT scan from the cylinder samples is presented in Fig. 6. The corresponding HUs are presented in Table 1. A range between -482 to 968 HUs was achieved. Lower HU values could be achieved in S15-S18. The printed grid was visible in the CT scan in some samples (e.g. S15 in Fig. 6), therefore, these samples

were excluded in this study. The resulting HU range correlates to radiodensities of the thorax patient including HU values of cortical bone to lungs (Table 1) [24,25]. The resulted CT scans (Fig. 7) using smaller pixel spacing including 0.5 mm, 0.4 mm and 0.3 mm as well as the CT scan with isotropic voxel size revealed that sample S14 also needs to be excluded in case smaller pixel spacing than 0.6 mm or isotropic voxels of 0.6 mm is required. However, the pixel spacing around 0.6 and slice thickness of 2 mm as used in this study (Fig. 6, Section 2.4) are one of the most common CT parameters used for different CT protocols in the clinic and that is why they were selected to be investigated in this study.

Table 2

The resulting average HU and standard deviation over all twenty-four replicas.

Sample	Mean (HU)	STD
S0	949.50	22.96
S1	646.60	28.47
S2	577.90	13.00
S3	483.20	25.80
S4	392.10	22.14
S5	302.60	18.01
S6	228.80	19.15
S7	97.83	20.36
S8	26.08	18.19
S9	-64.00	17.40
S10	-132.50	18.66
S11	-216.75	18.24
S12	-300.00	28.70

### 3.2 Resulting density for the replicas

The average HU and standard deviation for S0-S12 samples from the CT scan of the twenty-four cylinders (Figs. 5 b, c, d) are calculated and reported in Table 2. The mean HU values found over the replicas revealed a good reproduction of the original densities (Table 2). Axial and coronal slices of CT from all replicas presenting different wall thicknesses are also shown in Fig. 9 c, d.

### 3.3 Additively manufactured thorax phantom

The thorax phantom was successfully printed using the FDM printer and the pieces were glued together. (Fig. 8a-c).

### 3.4 Resulting density values for the thorax phantom

An axial slice from the patient and phantom CT are shown in Fig. 9 a, b. Based on the radiodensity analysis, the average density values achieved for the phantom CT at inner-bone areas for dorsal vertebral column, ventral vertebral body, rib cage and soft tissue were 166, -10, 99 and -93 HU, respectively. Our results showed a good agreement between different density values of the proposed phantom and the initial patient CT scan (target HUs) for these areas (Table 3).

#### 3.4.1 Resulting density range for the cortical bone

HU spectrum of the segmented cortical bone (Section 2.8) for both patient CT and the phantom CT are presented in Fig. 10. The density range for the segmented cortical bone for the patient and phantom was 230-1170 HU (Fig. 10a) and 230-910 HU (Fig. 10b), respectively. As a further analysis, we removed the values related to the extra part of the patients HU spectrum (910-1170 HU) from the segmentation (Fig. 10c). We observed that this part of the spectrum only includes a few percentages of the whole cortical bone segmentation and therefore no significant HU difference compared to results in

Fig. 10a could be achieved. These results confirmed that the dominant part of the bone segmentation spectrum is related to the 230-910 HU range which shows a good agreement in both phantom and the patient thorax skeleton CT.

### 3.5 Resulting physical dimensional comparison between the phantom and patient STL

The results from Extrema Analysis in 3-matic Research 13.0 showed that the average surface overlap between the skeletal parts was: 7% in the range of -7.00 to -4.10 mm; 60% in the range of -4.00 to -2.10 mm; 30% in the range of -2.00 to +0.00 mm; 2% in the range of 0.10 to 1.00 mm; 0.10% in the range of 1.10 to 2.00 mm; and 0.90% in the range of 2.10 to 9.00 mm. Negative bandwidth only indicates that the compared object (phantom STL) is within the target object (patient STL) (Fig. 11 a). The color code displaying the bandwidth of overlap (in mm) is as follows: indigo, turquoise, green, yellow, orange and red (Fig. 11 a). The results from Collision Detection in 3-matic Research 13.0 showed that the colliding volume was 80.33% for the rib cage, 95.71 for the vertebral body and 77.63% for the dorsal vertebral column with mean colliding volume of 84.56% (Fig. 11 b). The calculated volume is the sum of the volume of all the triangles that make up the structure under analysis (Fig. 4).

#### 3.5.1 Resulting wall thickness

The printed cortical bone/wall thicknesses were compared to the contour layer size (nominals) which was planned originally to print the walls and the error from nominals was calculated. On average, a good agreement between the printed cortical bone/wall thicknesses and their nominal values was achieved (Tables 4 and 5).

## 4 Discussion

3D printing is a promising technology for production of medical imaging phantoms which are required for staff training, device calibration, radiotherapy dosimetry and quality assurance (QA) purposes as well as evaluation and verification of advanced image processing techniques. In this study, the construction and properties of a CT-derived 3D printer generated thorax phantom with realistic bone-equivalent radiodensity were described. The generated thorax phantom geometry closely resembles a patient and includes direct manufacturing of bone structures while creating life-like heterogeneity within bone tissues.

The strong point of this study is the introduction of a workflow to produce an imaging phantom including complex thorax skeletal using single prints containing only one single filament with different densities. The wide range of HU achieved in this study enables the whole thorax phantom to be properly fabricated for clinical setting using only one commercially available filament and only one printer

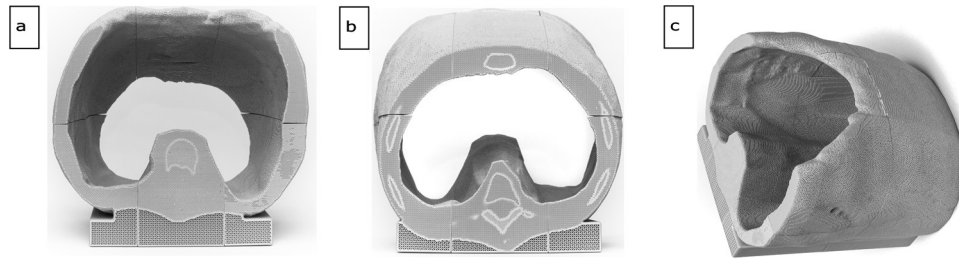


Figure 8. The 3D printed thorax phantom, a) Caudal-cranial and b) Cranial-caudal view of thorax phantom in supine position, (a, b) and longitudinal position (c).

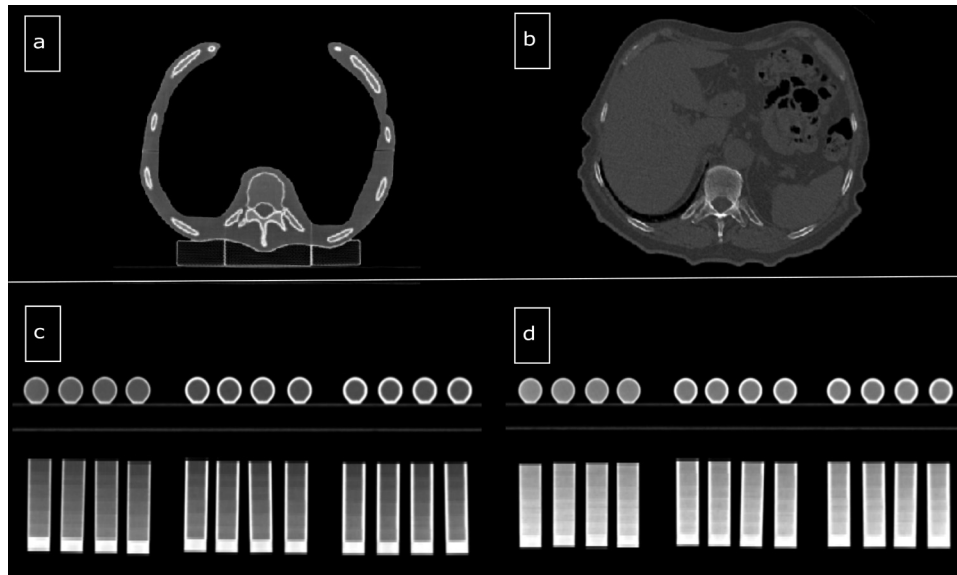


Figure 9. Representation of an axial slice of CT from the patient and the 3D printed phantom. Axial and coronal view from the CT scan from the printed cylinder replicas (Axial view only includes S12 (c, left) and S6 (d, right)). In (c) and (d) we have a contour thickness of 0.9 mm, 1.8 mm, 2.25 mm, each repeated for each 4 cylinders, from left, middle and right, respectively. The display window is set to the range [0,101–1154] HU.

Table 3

Resulting HU for the 3D printed phantom and its comparison with the patient densities at inner areas inside dorsal vertebral column, vertebral body, ribs and the soft tissue. Min: minimum, Max: maximum, Std: standard deviation.

Tissue	Patient HU				Phantom HU			
	Min	Max	Mean	Std	Min	Max	Mean	Std
Dorsal vertebral column	103	395	184	66	127	284	166	32
Vertebral body	-212	245	20	121	-24	6	-10	11
Rib	38	219	107	55	58	142	99	29
Soft tissue	-6	-131	-85	29	-72	-115	-93	12

device. The focus of this study was to replicate the density heterogeneity inside bone tissues of a thorax phantom; however, considering the HU range achieved (-482 to 968) the proposed technique could be properly used to print larger numbers of nominal infill densities also for organs, muscle, fat and lung enabling a full thorax phantom including realistic imaging properties of bone and soft tissues in the future.

Although simulating realistic bone-equivalence structure was a challenging goal for this study, promising results were achieved. First, the densities of the bone marrow in vertebral body and dorsal vertebral column and rib were in line with the observed density of patient thorax when imaged using the CT in kV range, suggesting inner-bone-equivalence for kV photons. The HU spectrum analysis revealed a good agreement between density range of the simulated cortical bone

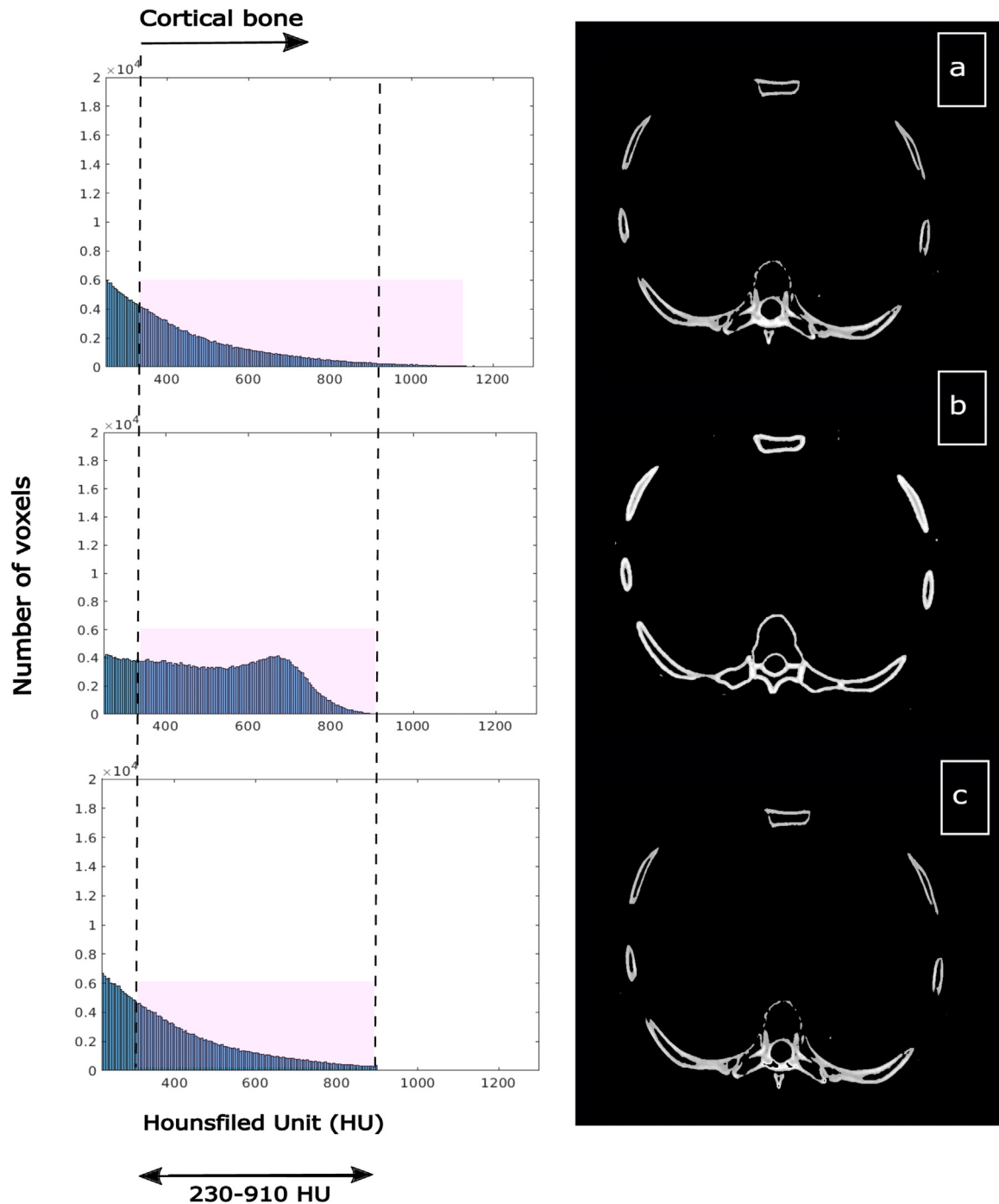


Figure 10. HU spectrum related to the cortical bone segmentation of a) the patient CT (230-1170 HU), b) phantom CT (230-910 HU), c) patient CT after removing the values related to the 910-1170 HU from the segmentation. The pink areas in left side show the HU range from which the cortical bone in the right side is segmented.

in the phantom CT compared to the real cortical bone in the patient thorax skeleton CT. Although the concentration of voxel values was different in spectrum from the patient and the phantom, the HU range for the cortical bone segmentation shows a good similarity between the patient and the phantom.

To our knowledge this study is the first demonstration which proposed direct fabrication of a realistic bone-like phantom for a full thorax skeleton. The only previous study, which also used FDM technology to develop an imaging thorax phantom, proposed printing of soft tissue-equivalence

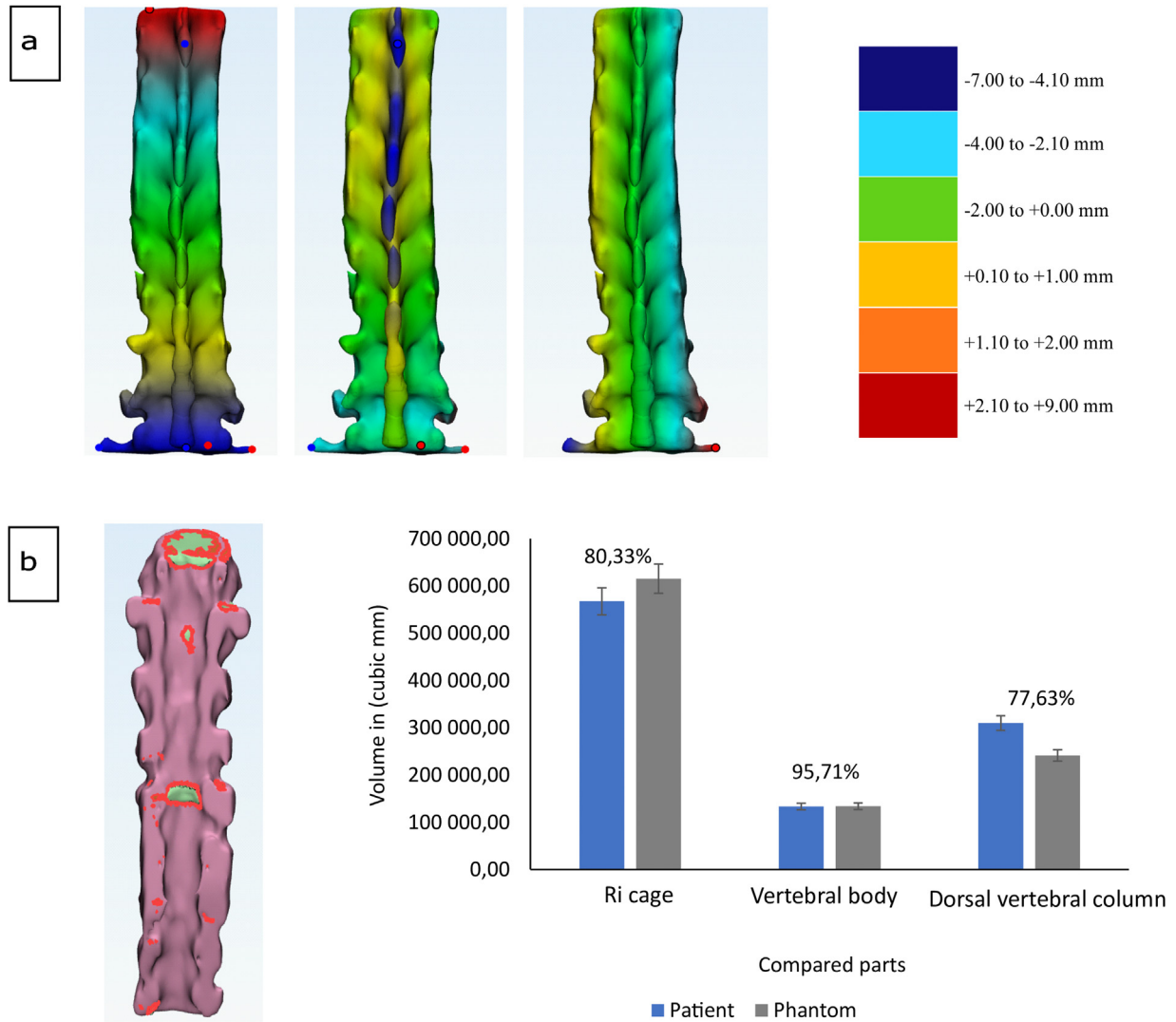


Figure 11. Results from physical dimensional comparison between the CT-derived patient and phantom STL, a) The result of surface overlap in Extrema analysis (in this case vertebral body, selected axis direction x (left), y (middle), z (right)), b) Pictorial and graphical representation of the results of the volume match in Collision detection is shown represented graphically. Collided triangles marked in pink on the target object.

Table 4

Cortical bone thickness results (average and standard deviation) related to the ventral vertebral body, rib cage and dorsal vertebral column and error calculation compared to the nominal values.

	Vertebral body [mm]	Rib cage [mm]	Dorsal vertebral column
Nominal value	0.9	1.8	2.25
Average	1.07	2.15	2.54
Standard deviation	0.37	0.25	0.33
Error	0.17	0.35	0.29

materials and non-direct reproduction of the bone density range (carved ribs with calcium sulfate) [20]. Our proposed thorax phantom outperforms previous studies proposing directly manufactured bone-equivalent thorax phantoms. The

simulated bone in the manufactured thorax phantom in [19] could not mimic the native bone regarding the HU values. Another limitation was regarding the design in which a single material was used for the entire bone structure which

Table 5

Wall thickness results (average and standard deviation) related to 24 cylinder replicas (8 cylinders with 0.9 mm contour, 8 cylinders with 1.8 mm contours, 8 cylinders with 2.25 mm contour).

	Cylinders with contour size of 0.9 mm	Cylinders with contour size of 1.8 mm	Cylinders with contour size of 2.25 mm
Average	1.10	1.95	2.50
Standard deviation	0.19	0.17	0.27
Error	0.20	0.15	0.25

led to a constant HU value for the whole bony structure. The simplicity of the bone model was therefore a limitation of this study. In another study [20] a higher HU was achieved compared to the previous study [19], but still the radiographic bone homogeneity due to single material filling process makes this approach far from simulating realistic bone. Another group [21] reported an average 731 HU over the whole bony structures. However, the average HU achieved was rather far from the average target patient bony density (HU = 371) reported in their study. In addition, infill parameters were fixed in the commercial 3D printer thus no control over the densities created for the bone structure was possible. Our research enhances those previous studies [19–21] by fabrication of realistic heterogeneity within bone structures, better HU agreement between the patient and phantom CT as well as achieving a wider HU range.

The proposed method in this study could also overcome the limitations reported by our previous study [4]. In the previous study [4], several steps were necessary for the manufacturing of bone structures, including 3D printing and cleaning a thorax phantom, creating a radiopaque mixture at different ratios and filling the skeletal structure at different stages. The major advantage of the current study is the introduction of a method to directly manufacture bone-like phantoms. This eliminates the need for multiple processing stages and can therefore reduce the errors happening during the fabrication chain, such as incomplete removal of the support structure, or the generation of air bubbles during the filling process due to limited access to the areas inside the phantom. In addition, in the previous study there was no possibility to mimic the internal bone structures, including cortical and bone marrow, only the average HU value of the corresponding bones could be mimicked. In contrast, in the current study, the use of filament printing technology enables simulation of the wall thickness of cortical bone by the number of perimeters, as well as of different bone densities of cancellous bone by variation of the infill density. In addition, with this method, a much higher density range was achieved (–482 to 968 HU) compared to the previous work (42 to 705 HU) which can enable fabrication of the full thorax phantom including bone and soft tissues as well as the lung at a single print by simply changing the infill density parameter of the print.

Our approach could also outperform previous studies, in which realistic bone-equivalency for phantoms from other anatomical sites other than thorax were the main objective.

In a study [22] a HU range of 56 to 1102 was achieved for the soft and bony tissues using two different filament and a dual-extrusion printing. The densities within the range of  $56 \pm 30$  HU for soft tissues,  $1102 \pm 182$  HU for cortical,  $400 \pm 64$  HU for cancellous and  $173 \pm 62$  HU for red bone marrow were achieved for a patient-specific femur phantom to mimic realistic heterogeneity inside the bone tissue. In this study, although realistic heterogeneity inside the bone tissue was simulated, which makes this method a sufficient approach to fabricate real bones for imaging, a discrepancy was observed in the achieved mean HU for different manufactured bone parts compared to the target HUs. The reason for such discrepancies was the inherent high-density metallic shells used for the printed bone phantom as well as the inherent printing defects of dual-extrusion 3D printing while extrusion of metallic reinforced compounds. This eventually produced several surface defects leading beam hardening artefacts in the CT image. The wider achieved HU range and the single-filament requirement used for proposed approach are two advantages of our method compared to the two previous studies [8,22]. Our approach facilitates a simpler printing process in order to simulate complexity inside bone tissues and also the wider HU range achieved helps a simultaneous print of both bone tissue and soft tissues within a single print. In addition, a better agreement between the target density (patient) and the simulated density (phantom) for bone marrow was achieved with our approach compared to the study in [22]. Our results using a patient dataset confirmed that the mean HU value can be reproduced within an error up to 30 HU using our approach. In addition, the deviation found in the target HU values were much smaller compared to the patient data HU deviation. We expect these values to be even smaller if compared to a larger cohort of patient data.

Our results showed the filament printing technology using StoneFil filament is a more suitable method for manufacturing realistic bone phantoms when compared to other widely used 3D printing technology such as PolyJet technology. Available PolyJet materials have low density in the range of human soft tissue HU values [19,26] which limit their use in direct fabrication of imaging phantoms including cortical bone. In addition, using PolyJet technology, each material leads to a single radiodensity in the printed sample and therefore a distinct radiodensity spectrum can only be achieved depending on the availability of printable materials. One of advantages of FDM technology over the PolyJet technology is the ability

where a single material can reproduce a wide variety of HU of human bone and soft tissues in CT by altering infill density parameter of the printer, therefore simplifying the fabrication process.

The physical dimensional comparison using both Extrema Analysis and Collision Detection methods confirmed a mean surface overlap of 90% (for the bandwidth of -4.00 to +0.00 mm) and a mean volumetric overlap of 84,56% between the patient and phantom STL model. The mismatch (specially in rib cage and dorsal vertebral column) was based on (1) software limitations of the contrast-based segmentation process, (2) smaller printing platform necessitated printing of the phantom in multiple parts that were ultimately glued together; therefore, minor alignment errors during the gluing process prevented a complete digital overlap of the STLs during dimensional comparison, (3) post-printing polymerization shrinkage has also been known to cause minor dimensional errors.

Reproducibility test results also confirmed a good agreement between the HU values of the replicas compared to those initial samples. The wall thickness analysis also revealed a good match between the printed cylinder walls/cortical walls in the thorax phantom as compared to the planned nominal values.

We acknowledge some limitations of our developed thorax phantom. We printed the spine as one structure and not as individual vertebrae; this could be improved using a CT scan with smaller slice thickness size when creating the printing model and also by means of an exact manual segmentation. For the printing of the phantom, the thorax had to be separated into several parts to fit onto the building platform; however, this is a limitation of our current available printer device. A single print without requirement to print division is feasible using the available commercial FDM printer device with working area of 50 cm<sup>3</sup> (e.g. Rat Rig V-Core 3 [27]). This will also help preventing errors stemming from geometry mismatch due to gluing different parts. One perspective for our future work will include modifying the model to integrate individual vertebrae in order to design a more precise model. In addition, the possibility for printing a full thorax phantom, including both soft and bony tissue with realistic heterogeneity in the CT scan, will be investigated.

## 5 Conclusion

Our results based on the printed phantom as well as based on reproducibility tests showed a good agreement between the resulting HU and target densities in the patient thorax CT. We demonstrated that using one filament, while only varying the infill density, a wide range of HU were replicated enabling 3D printing phantom construction in single prints, while simulating complex heterogeneity within bone tissues inside a thorax skeleton.

## Declaration of Competing Interest

The authors declare that they have no known competing financial interests or personal relationships that could have appeared to influence the work reported in this paper.

## Acknowledgements

This work has been supported by ACMIT – Austrian Center for Medical Innovation and Technology, which is funded within the scope of the COMET program and funded by Austrian BMVIT and BMWFV and the governments of Lower Austria and Tyrol. This work was also supported by the Provincial Government of Lower Austria (Land Niederösterreich) under grant assignment number WST3-F2-528983/005-2018. Part of this research has been supported by the M3dRES project infrastructure (Grant No. 858060), Austrian Research Promoting Agency (FFG).

## References

- [1] Filippou V, Tsoumpas C. Recent advances on the development of phantoms using 3D printing for imaging with CT, MRI, PET, SPECT, and ultrasound. *Med. Phys* 2018;45:740–60, <http://dx.doi.org/10.1002/mp.13058>.
- [2] White D. The design and manufacture of anthropomorphic phantoms. *Radiat. Prot. Dosim* 1993;49:359–69, <http://dx.doi.org/10.1093/rpd/49.1-3.359>.
- [3] Hazelaar C, van Eijnatten M, Dabele M, Wolff J, Forouzanfar T, Slotman B, et al. Using 3D printing techniques to create an anthropomorphic thorax phantom for medical imaging purposes. *Med. Phys* 2018;45:92–100, <http://dx.doi.org/10.1002/mp.12644>.
- [4] Hatamikia S, Oberoi G, Unger E, Kronreif G, Kettenbach J, Buschmann M, et al. Additively manufactured patient-specific anthropomorphic thorax phantom with realistic radiation attenuation properties. *Front. Bioeng. Biotechnol* 2020;8:385, <http://dx.doi.org/10.3389/fbioe.2020.00385>.
- [5] Homolka P, Figl M, Wartak A, Glanzer M, Dünkelmeyer M, Hojreh A, et al. Design of a head phantom produced on a 3D rapid prototyping printer and comparison with a RANDO and 3 M lucite head phantom in eye dosimetry applications. *Phys. Med. Biol* 2017;62:3158–74, <http://dx.doi.org/10.1088/1361-6560/aa602c>.
- [6] Tino R, Yeo A, Leary M, Brandt M, Kron T. A systematic review on 3D-printed imaging and dosimetry phantoms in radiation therapy. *Technol. Cancer. Res. Treat* 2019;18, <http://dx.doi.org/10.1177/1533033819870208>, 153303381987020.
- [7] Hatamikia S, Biguri A, Kronreif G, Kettenbach J, Russ T, Furtado H, Kumar Shiyam L, et al. Optimization for customized trajectories in Cone Beam Computed Tomography. *Med. Phys* 2020;47:4786–99, <http://dx.doi.org/10.1002/mp.14403>.
- [8] Okkalidis N, Marinakis G. Technical note: Accurate replication of soft and bone tissues with 3d printing. *Med. Phys* 2020;47:2206–11, <http://dx.doi.org/10.1002/mp.14100>.
- [9] Li F, Engelmann R, Pesce L, Armato SG3rd, Macmahon H. Improved detection of focal pneumonia by chest radiography with bone suppression imaging. *Eur. Radiol* 2012;22:2729–35, <http://dx.doi.org/10.1007/s00330-012-2550-y>.

- [10] Birkfellner W, Stock M, Figl M, Kettenbach J, Georg D, Bergmann H. Stochastic rank correlation: a robust merit function for 2D/3D registration of image data obtained at different energies. *Med Phys* 2009;36:3420–8, <http://dx.doi.org/10.1118/1.3157111>.
- [11] Sharma N, Aggarwal LM. Automated medical image segmentation techniques. *J. Med. Phys* 2010;35:3–14, <http://dx.doi.org/10.4103/0971-6203.58777>.
- [12] Holmes RB, Negus IS, Wiltshire SJ, Thorne GC, Young P. Creation of an anthropomorphic ct head phantom for verification of image segmentation. *Med. Phys* 2020;47:2380–91, <http://dx.doi.org/10.1002/mp.14127>.
- [13] Niebuhr NI, Johnen W, Güldaglar T, Runz A, Echner G, Mann P, et al., Technical note: Radiological properties of tissue surrogates used in a multimodality deformable pelvic phantom for mr-guided radiotherapy. *Med. Phys* 2016;43:908–16, <http://dx.doi.org/10.1118/1.4939874>.
- [14] Niebuhr NI, Johnen W, Echner G, Runz A, Bach M, Stoll M, et al. The ADAM-pelvis phantom—an anthropomorphic, deformable and multimodal phantom for MRgRT. *Phys. Med. Biol* 2019;64:04NT05, <http://dx.doi.org/10.1088/1361-6560/aafd5f>.
- [15] Andrade M, Potiens M. Commercial filament testing for use in 3d printed phantoms. *Radiat. Phys. Chem* 2020;174:108906, <http://dx.doi.org/10.1016/j.radphyschem.2020.108906>.
- [16] Ceh J, Youd T, Mastrovich Z, Peterson C, Khan S, Sasser TA, et al. Bismuth infusion of ABS enables additive manufacturing of complex radiological phantoms and shielding equipment. *Sensors* 2017;17(459), <http://dx.doi.org/10.3390/s17030459>.
- [17] Hamedani BA, Melvin A, Vaheesan K, Gadani S, Pereira K, Hall AF. Three-dimensional printing ct-derived objects with controllable radiopacity. *J. Appl. Clin. Med. Phys* 2018;19:317–28, <http://dx.doi.org/10.1002/acm2.12278>.
- [18] Kairn T, Zahrani M, Cassim N, Livingstone AG, Charles PH, Crowe SB. Quasi- simultaneous 3d printing of muscle-, lung- and bone-equivalent media: a proof-of-concept study. *Phys. Eng. Sci. Med* 2020;43:701–10, <http://dx.doi.org/10.1007/s13246-020-00864-5>.
- [19] Mayer R, Liacouras P, Thomas A, Kang M, Lin L, Simone CB. 3D printer generated thorax phantom with mobile tumor for radiation dosimetry. *Rev. Sci. Instrum* 2015;86:74301, <http://dx.doi.org/10.1063/1.4923294>.
- [20] Pallotta S, Calusi S, Foggi L, Lisci R, Masi L, Marrazzo L. ADAM: a breathing phantom for lung SBRT quality assurance. *Phys. Med* 2018;49:147–55, <http://dx.doi.org/10.1016/j.ejmp.2017.07.004>.
- [21] Hazelaar C, Eijnatten M, Dahele M, Wolff J, Forouzanfar T, Slotman B. Using 3D printing techniques to create an anthropomorphic thorax phantom for medical imaging purposes. *Med Phys* 2018;45:92–100, <http://dx.doi.org/10.1002/mp.12644>.
- [22] Neumann W, Lietzmann F, Schad LR, Zöllner FG. Design of a multimodal (1H/23Na MR/CT) anthropomorphic thorax phantom. *Z. Med. Phys* 2017;27:124–31, <http://dx.doi.org/10.1016/j.zemedi.2016.07.004>.
- [23] Rance T, Yeo A, Brandt M, Leary M, Kronc T. The interlace deposition method of bone equivalent material extrusion 3D printing for imaging in radiotherapy. *Mater. Design* 2021;199:109439, <http://dx.doi.org/10.1016/j.matdes.2020.109439>.
- [24] Npraveen B, Sanjana P, Keerthi G, Ashubhasini R, Shubha G. Comparison of gray values of cone-beam computed tomography with hounsfield units of multislice computed tomography: An in vitro study. *Indian. J. Dent. Res* 2017;28:66–70, [http://dx.doi.org/10.4103/ijdr.IJDR\\_415\\_16](http://dx.doi.org/10.4103/ijdr.IJDR_415_16).
- [25] Chougule VN, Mulay AV, Ahuja BB. Clinical Case Study: Spine Modeling for Minimum Invasive Spine Surgeries (MISS) using Rapid Prototyping. *Proceedings of 10<sup>th</sup> International conference on Precision, Meso, Micro and Nanoengineering (COPEN10)*. December 07–09 2017.
- [26] Neumann W, Pusch TP, Siegfarth M, Schad LR, Stallkamp JL. CT and MRI compatibility of flexible 3D-printed materials for soft actuators and robots used in image-guided interventions. *Med. Phys* 2019;46:5488–98, <http://dx.doi.org/10.1002/mp.13852>.
- [27] Rat Rig company. <https://www.ratrig.com/>.
- [28] <http://www.slicer.org>.
- [29] Fedorov A, Beichel R, Kalpathy-Cramer J, Finet J, Fillion-Robin J-C, Pujol S, Bauer C, Jennings D, Fennessy F, Sonka M, Buatti J, Aylward SR, Miller JV, Pieper S, Kikinis R. 3D Slicer as an Image Computing Platform for the Quantitative Imaging Network. *Magnetic Resonance Imaging* 2012;30(9):1323–41. PMID: 22770690.

Available online at [www.sciencedirect.com](http://www.sciencedirect.com)

**ScienceDirect**